JCI insight

Store-operated Ca^{2+} entry controls ameloblast cell function and enamel development

Miriam Eckstein,[1] Martin Vaeth,[2] Cinzia Fornai,[3,4] Manikandan Vinu,[5] Timothy G. Bromage,[1,6] Meerim K. Nurbaeva,[1] Jessica L. Sorge,[1] Paulo G. Coelho,[6] Youssef Idaghdour,[5] Stefan Feske,[2] and Rodrigo S. Lacruz[1]

[1]Department of Basic Science and Craniofacial Biology, New York University College of Dentistry, New York, New York, USA. [2]Department of Pathology, New York University School of Medicine, New York, New York, USA. [3]Department of Anthropology, University of Vienna, Vienna, Austria. [4]Department of Evolutionary Medicine, University of Zurich, Zurich, Switzerland. [5]Biology Program, Division of Science and Mathematics, New York University Abu Dhabi, Abu Dhabi, United Arab Emirates. [6]Department of Biomaterials and Biomimetics, New York University College of Dentistry, New York, New York, USA.

Loss-of-function mutations in stromal interaction molecule 1 (STIM1) impair the activation of Ca^{2+} release–activated Ca^{2+} (CRAC) channels and store-operated Ca^{2+} entry (SOCE), resulting in a disease syndrome called CRAC channelopathy that is characterized by severe dental enamel defects. The cause of these enamel defects has remained unclear given a lack of animal models. We generated *Stim1/2^{K14cre}* mice to delete STIM1 and its homolog STIM2 in enamel cells. These mice showed impaired SOCE in enamel cells. Enamel in *Stim1/2^{K14cre}* mice was hypomineralized with decreased Ca content, mechanically weak, and thinner. The morphology of SOCE-deficient ameloblasts was altered, showing loss of the typical ruffled border, resulting in mislocalized mitochondria. Global gene expression analysis of SOCE-deficient ameloblasts revealed strong dysregulation of several pathways. ER stress genes associated with the unfolded protein response were increased in *Stim1/2*-deficient cells, whereas the expression of components of the glutathione system were decreased. Consistent with increased oxidative stress, we found increased ROS production, decreased mitochondrial function, and abnormal mitochondrial morphology in ameloblasts of *Stim1/2^{K14cre}* mice. Collectively, these data show that loss of SOCE in enamel cells has substantial detrimental effects on gene expression, cell function, and the mineralization of dental enamel.

Introduction

Amelogenesis, or enamel formation, involves two main stages, termed secretory and maturation or mineralization stages. Ameloblast cells derive from ectodermal epithelium and are responsible for forming and mineralizing enamel. In the secretory stage, they provide an organic template for enamel crystal growth, which is then mineralized during the maturation stage. This latter stage can be further divided into two discrete cell populations, namely ruffled and smooth ameloblasts, based on morphology, which has an effect on ionic transport (1, 2). These changes reflect the complex nature of amelogenesis, a process compounded by the fact that ameloblasts are nondividing cells. As a result, enamel, unlike bone, does not remodel.

The enamel hydroxyapatite-like crystals form de novo by precipitation of ions in the enamel space isolated by a semipermeable barrier formed by ameloblasts (3). These crystals contain large quantities of Ca^{2+} that are transferred from the blood to the enamel space by the ameloblasts. This dependency on Ca^{2+} is critical because crystal formation requires a steady supply of Ca^{2+}. Ameloblasts, thus, handle bulk Ca^{2+} without causing irreparable cell stress (4). However, how Ca^{2+} is transported by these cells and the role of Ca^{2+} as an intracellular second messenger in enamel cells remains poorly understood (3). This has resulted in clinical phenotypes that are linked with Ca^{2+} deficiency being more commonly associated with skeletal diseases (i.e., osteoporosis, osteopenia), but how Ca^{2+} deficit affects enamel is less clear.

Conflict of interest: S. Feske is a cofounder of CalciMedica Inc.

Submitted: October 11, 2016
Accepted: February 2, 2017
Published: March 23, 2017

Reference information:
JCI Insight. 2017;2(6):e91166. https://doi.org/10.1172/jci.insight.91166.

An important Ca^{2+} channel in nonexcitable cells, such as ameloblasts, is the Ca^{2+} release–activated Ca^{2+} (CRAC) channel, which mediates store-operated Ca^{2+} entry (SOCE). CRAC channel activation requires depletion of Ca^{2+} from intracellular stores, mainly the ER, which is detected as a reduction in the ER Ca^{2+} concentration ($[Ca^{2+}]_{ER}$) by stromal interaction molecule 1 (STIM1) and its homolog STIM2, which are located in the ER membrane. Upon reduction of $[Ca^{2+}]_{ER}$, STIM1 and STIM2 undergo a conformational change that allows them to bind to and activate ORAI proteins in the plasma membrane. ORAI1 and its homologs ORAI2 and ORAI3 are tetraspanning plasma membrane proteins that form the pore of the CRAC channel and mediate SOCE (5, 6). STIM1, STIM2, and the Ca^{2+} channel proteins ORAI1, ORAI2, and ORAI3 are present in many cells, including enamel cells, as recently reported (7, 8).

Recent studies have shed light on the links between Ca^{2+} and enamel when patients with immune system dysfunction, caused by impaired SOCE, showed an abnormal enamel phenotype, characterized as amelogenesis imperfecta*,* with hypomineralized enamel that wears extremely rapidly (9–11). At least 4 loss-of-function (LoF) mutations in *STIM1* and 4 LoF mutations in *ORAI1* severely affect enamel to the point of near-complete loss of the enamel in the erupted teeth in most cases (12). The clinical data available from these patients indicate that both primary and permanent teeth are severely affected, impairing the patients' capacity to break down food and requiring extensive reconstructive dental surgery. All LoF mutations in STIM1 and ORAI1 were shown to result in severely impaired or absent SOCE in fibroblasts or immune cells (12). Besides amelogenesis imperfecta*,* the clinical phenotype of these patients is characterized by severe immunodeficiency resulting in frequent viral and bacterial infections, autoimmunity, muscular hypotonia, and sweat gland dysfunction (12, 13). Teeth from these patients have not been available for study of the structural and molecular enamel defects, and, hence, it has not been possible to assess the full effect of SOCE deficiency on enamel development. Moreover, the currently available animal models with impaired SOCE have been of limited use, as deletion of *Orai1*, *Stim1*, or both *Stim1*/*Stim2* genes results in perinatal lethality of mice (14). To solve this issue, we made use of mice with conditional deletion of *Stim1*/*Stim2* in ectodermal tissues, including enamel cells.

We report that enamel cells derived from *Stim1*/*Stim2*-deficient mice showed significantly reduced SOCE. The dental phenotype of these mice included severe hypomineralization of their enamel, with lower Ca levels as well as thinner and softer enamel that wore rapidly, showing a remarkable similarity to the human dental phenotype. Loss of STIM1 and STIM2, furthermore, resulted in significant defects in gene expression, which were associated with dysregulated ER stress and oxidative stress response as well as changes in mitochondrial function and morphology. We propose that SOCE mediated by STIM1 and STIM2 is critically important for both the mineralization of dental enamel and the regulation of gene expression in ameloblasts and thus cell function.

Results

Tissue-specific deletion of Stim1 and Stim2. To address the effect of SOCE deficiency in enamel, we used mice with conditional deletion of *Stim1* and *Stim2* in keratin expressing ectodermally derived tissues, such as epidermis, salivary glands, and dental enamel, that were generated as described previously (13). Enamel organ (EO) cells isolated from *Stim1*$^{fl/fl}$ *Stim2*$^{fl/fl}$ *K14Cre* (herein referred to as *Stim1/2*^{K14cre}) mice showed drastically reduced mRNA levels of *Stim1* and *Stim2* relative to control cells, as expected (Figure 1A). To further confirm deletion of protein expression*,* tissues from 5-week-old WT controls and *Stim1/2*^{K14cre} mice were isolated for immunohistochemical analysis. Our previous immunofluorescence studies reported that secretory-stage ameloblasts do not express STIM1 (15); therefore, we imaged only maturation-stage ameloblasts. Cells from WT mice showed a strong STIM1 signal, whereas no signal was identified in maturation-stage ameloblasts of *Stim1/2*^{K14cre} mice (Figure 1B). Other tissues expected to lack STIM1 in *Stim1/2*^{K14cre} mice, including keratinocytes in the epidermis and salivary gland cells, showed no immunoreactivity, whereas STIM1 signals were readily detected in tissues of WT control animals (Figure 1B). In contrast, tissues that were not expected to lack STIM1, such as muscle or brain, showed STIM1 expression by immunohistochemistry in both *Stim1/2*^{K14cre} and WT control mice (Figure 1B). These data confirm the specificity of *Stim1* and *Stim2* deletion in ectodermal-derived tissues, including ameloblasts of *Stim1/2*^{K14cre} mice.

Abnormal SOCE in enamel cells from Stim1/2^{K14cre} *mice*. Having confirmed lack of STIM1 expression in ameloblasts, we tested whether SOCE was affected in these cells. EO cells were isolated from 8- to 10-week-old *Stim1/2*^{K14cre} mice and WT littermates following protocols previously described (15). To maximize the number of cells to be used for Fura-2 measurements, we did not separate secretory- from maturation-stage

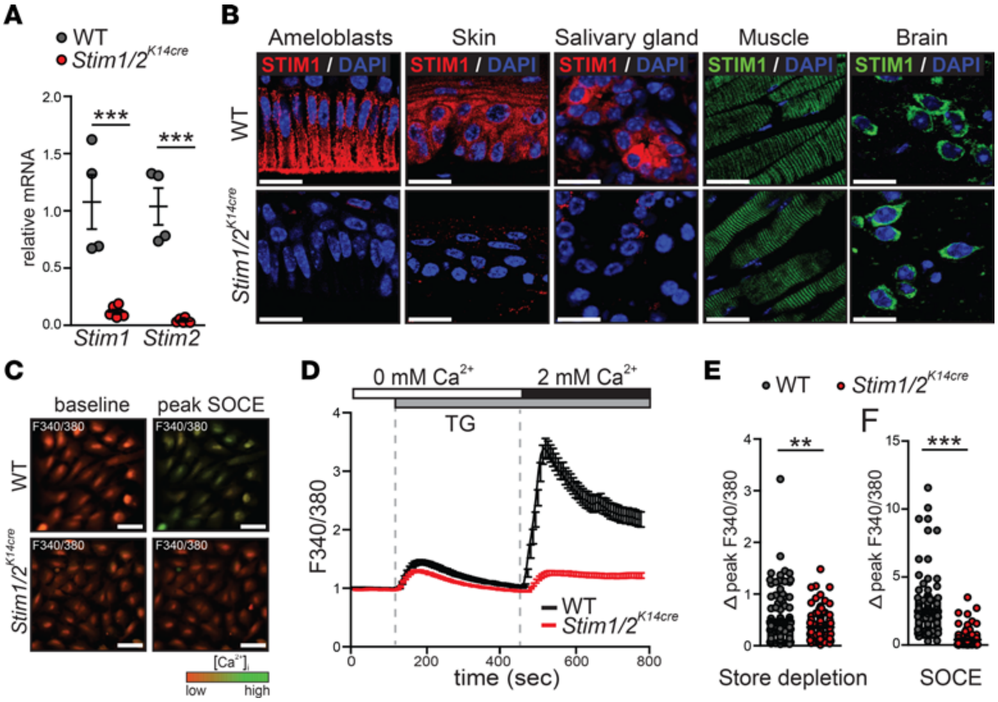

Figure 1. STIM1 and STIM2 mediate store-operated Ca^{2+} entry in ameloblast cells. (**A**) Analysis of *Stim1* and *Stim2* gene expression in enamel organ (EO) cells of WT and *Stim1/2*^{K14cre} mice by qRT-PCR showing significantly decreased levels of both transcripts in the latter. Data represent mean (± SEM) of *n* = 4 WT and *n* = 6 *Stim1/2*^{K14cre} mice (****P* < 0.001, 2-tailed unpaired Student's *t* test). (**B**) STIM1 protein expression in maturation-stage ameloblasts, endothelial cells, salivary glands, muscle, and brain of WT and *Stim1/2*^{K14cre} mice by immunofluorescence. Strong positive reactions were detected in all WT tissues, whereas STIM1 signals were found only in nonkeratin 14 targets (i.e., muscle and brain). Scale bar: 20 μm. (**C–F**) Conditional deletion of *Stim1* and *Stim2* genes drastically diminishes store-operated Ca^{2+} entry (SOCE) in ameloblast cells. EO cells isolated from WT and *Stim1/2*^{K14cre} mice were loaded with Fura-2-AM and intracellular Ca^{2+} concentrations ([Ca^{2+}]$_i$) were determined by time-lapse microscopy after thapsigargin (TG) stimulation and readdition of 2 mM Ca^{2+}. (**C**) Representative images of EO cells from WT and *Stim1/2*^{K14cre} mice showing the F340/380 fluorescence ratio before stimulation with TG in Ca^{2+}-free medium (5 seconds) (baseline) and after addition of 2 mM Ca^{2+} (490 seconds) (peak SOCE). Scale bar: 20 μm. (**D–F**) Upon stimulation with TG (1.25 μM), *Stim1/2*^{K14cre} EO cells (red tracings) showed significant differences in ER Ca^{2+} release and Ca^{2+} entry relative to controls (black tracings). Data were normalized by setting baseline to 1. Statistical analysis of average delta peak for TG-induced store depletion and for Ca^{2+} entry are shown in **E** and **F**, respectively. Data in **D–F** represent mean ± SEM from *n* = 5 different experiments. Each experiment sampled cells obtained from 1 WT mouse and 1 *Stim1/2*^{K14cre} littermate. Total cells: WT = 132, *Stim1/2*^{K14cre} = 126. (***P* < 0.005, ****P* < 0.001, 2-tailed unpaired Student's *t* test).

EO cells and pooled cells from both stages. EO cells from WT mice stimulated with thapsigargin to passively deplete the ER stores in the absence of extracellular Ca^{2+} showed a moderate increase in [Ca^{2+}]$_i$, which was reduced in EO cells isolated from *Stim1/2*^{K14cre} mice (Figure 1, C–E). Readdition of extracellular Ca^{2+} to WT cells resulted in a strong rise in [Ca^{2+}]$_i$, consistent with SOCE, as expected (Figure 1, C, D, and F). By contrast, EO cells from *Stim1/2*^{K14cre} mice showed drastically reduced SOCE upon readdition of Ca^{2+}. These findings demonstrate that STIM1 and STIM2 are essential for SOCE in ameloblasts.

Altered enamel phenotype in SOCE-deficient mice. To assess the effect of loss of STIM1/STIM2 in enamel, we conducted a detailed examination of the dentition in *Stim1/2*^{K14cre} mice. Gross visual examination of the incisors of *Stim1/2*^{K14cre} mice showed an abnormal chalky-white appearance (Figure 2A), which is often associated with hypomineralization or enamel loss (16). To further detail the enamel phenotype of these mice, we imaged different tooth types using a variety of microscopy and tomographic techniques.

First, we investigated teeth of *Stim1/2*^{K14cre} mice and WT littermates by micro–computerized tomography. Hemimandibles were scanned at a resolution of 13 μm and reconstructed for 3D modeling (Figure 2B). *Stim1/2*^{K14cre} mice showed a general loss of enamel (colored in red in Figure 2B) in all teeth. Enamel thickness, a surrogate measure of normal ameloblast function, was determined using virtual imaging in two ways. First, we measured linear enamel thickness in similar regions of the teeth in the enamel just below and anterior to the first molar (M1) (Supplemental Figure 1, A and B; supplemental material available online with this article; https://doi.org/10.1172/jci.insight.91166DS1). Second, we analyzed the total volume of enamel in the incisors relative to the area covered by the dentine by using 3

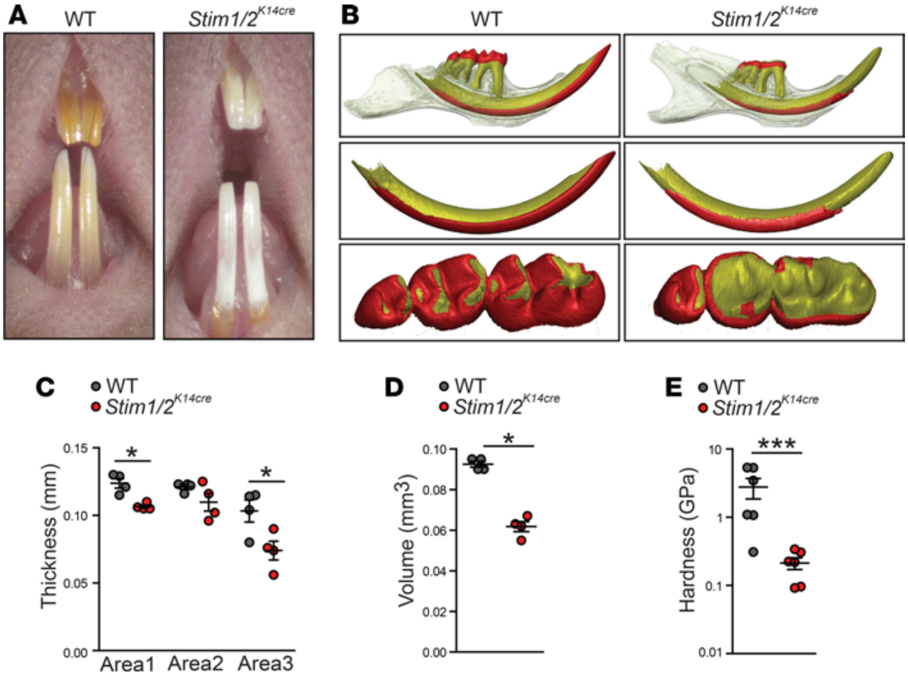

Figure 2. *Stim1/2*^{K14cre} mice show abnormal enamel. (**A**) Gross examination of the dental phenotype shows abnormal (chalky-white) appearance on incisors of *Stim1/2*^{K14cre} mice compared with WT littermates. These changes were characteristic of all *Stim1/2*^{K14cre} mice analyzed in this study. (**B**) Micro–computerized tomography analysis shows loss of enamel tissue (color-coded red) in *Stim1/2*^{K14cre} mice relative to WT littermates in incisors and molars. Dentine is widely exposed on the occlusal surface of all molars in *Stim1/2*^{K14cre} mice. $n = 3$ mice per group. (**C**) Incisor linear enamel thickness measured in 3 different regions of interest. The region of interest is located below the first molar. *Stim1/2*^{K14cre} mice show reduced linear enamel thickness in 2 of 3 three areas (areas 1 and 3) (see Supplemental Figure 1). Data represent mean ± SEM of $n = 4$ mice per group (*$P < 0.05$, **$P < 0.005$, 1-way ANOVA); however, only the differences in area 1 remains statistically significant after applying Bonferroni correction for multiple comparisons ($P < 0.016$). (**D**) Total enamel volume was also decreased in *Stim1/2*^{K14cre} mice (mean ± SEM of $n = 4$ mice per group; *$P < 0.05$, 2-tailed unpaired Student's *t* test). (**E**) Microhardness analysis showed significantly softer enamel in *Stim1/2*^{K14cre} incisor enamel compared with controls. Test site is shown in Supplemental Figure 1A. Data represent mean (± SEM) of $n = 6$ mice per group (***$P < 0.0001$, 2-tailed unpaired Student's *t* test).

interpolating planes (Supplemental Figure 1C). Results showed that *Stim1/2*^{K14cre} mice had reduced linear enamel thickness and decreased enamel volume compared with WT controls (Figure 2, C and D). Next, we investigated the load resistance of teeth using microhardness analysis. Teeth from WT and *Stim1/2*^{K14cre} mice were measured using a microprobe in multiple areas of the same regions of the incisors (Supplemental Figure 1, A and B). When probing enamel using the same load, the enamel of *Stim1/2*^{K14cre} mice was significantly softer than that of WT littermates (Figure 2E), indicating that its mechanical performance is extremely weak.

To compare mineralization differences in the incisor enamel at the unerupted area below the M1 (Supplemental Figure 1A), we used backscattered electron imaging using scanning electron microscopy (BSE-SEM). We detected very weak signals by BSE-SEM in the enamel of *Stim1/2*^{K14cre} mice, indicating substantial hypomineralization (Figure 3, A and B). To further analyze these differences, we assessed changes in elemental composition in enamel using energy dispersive x-ray spectroscopy (EDAX). Results showed that the enamel of *Stim1/2*^{K14cre} mice was Ca deficient, with a loss of approximately 50% of the Ca found in WT controls (Supplemental Table 1). Other key elements present in mineralized enamel, such as P, were approximately 24% lower in *Stim1/2*^{K14cre} mice than in controls.

Differences in the rod-interrod pattern can be a proxy for changes in the depositional pattern of enamel matrix or alterations in ameloblast movement. SEM in secondary electron mode showed that *Stim1/2*^{K14cre} mice had normal enamel rod patterns (Figure 3, C and D). Moreover, the number of cusps in each molar, which is established during the embryonic period and may indicate early developmental disruptions in tooth formation, was the same in *Stim1/2*^{K14cre} and WT mice (Figure 3, E and F), indicating normal cusp development. However, *Stim1/2*^{K14cre} mice showed advanced enamel wear (attrition) in the entire molar row relative to WT controls (Figure 3, E and F). The outer enamel in the molars of *Stim1/2*^{K14cre} mice was severely hypoplastic, with noticeable cracks (Figure 3, G and H). These data combined demonstrate that *Stim1/2*^{K14cre} mice formed enamel but that it was lost early on. This was due to important mineral deficiencies that rendered the enamel mechanically weak, resulting in rapid wear.

Changes in Ca^{2+} *homeostasis in Stim1/2*^{K14cre} *mice*. To assess the potential effects that dysregulation of SOCE had in Ca^{2+} homeostasis, we evaluated the expression of a number of genes associated with Ca^{2+} mobilization in enamel cells by qRT-PCR. Sarco-endoplasmic reticulum Ca^{2+}-ATPase 2 (SERCA2) pumps cytosolic Ca^{2+} into the ER lumen, thereby participating in Ca^{2+} homeostasis. In enamel cells from *Stim1/2*^{K14cre} mice, we observed an increased expression of the main SERCA isoform (coded by *Atp2a2*) expressed by ameloblasts (Figure 4A). More critically, considering the potential effect of a reduction in Ca^{2+} entry on the extrusion system, we focused our attention on exchangers that participate in Ca^{2+} extrusion in enamel cells. No significant changes were observed in the Ca^{2+} exchangers of the NCX family (coded by *Slc8a* genes) expressed in enamel cells (Figure 4A). However, the most essential

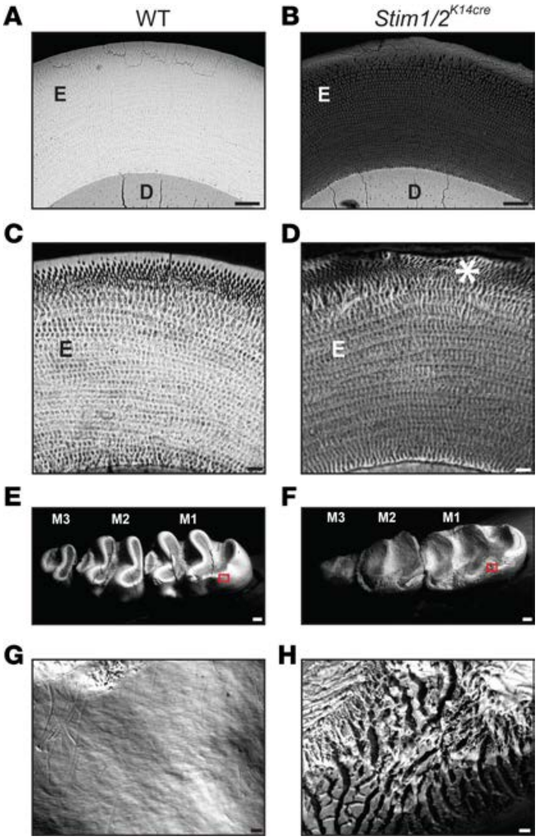

Figure 3. *Stim1/2*^{K14cre} mice show hypomineralized enamel. (**A** and **B**) Backscattered scanning electron microscopy (BSE) analyses of incisor cross-sections isolated from WT (**A**) and *Stim1/2*^{K14cre} mice (**B**) sampled just below the anterior first lower molar (M1) (see also Supplemental Figure 1) showing diminished BSE signals in the enamel in *Stim1/2*^{K14cre} mice, consistent with severe hypomineralization ($n = 3$ mice per group). (**C** and **D**) Representative scanning electron microscopy (SEM) micrographs in secondary electron mode of the same mice showing normal rod-interrod microstructure in the WT (**C**) and *Stim1/2*^{K14cre} mouse enamel (**D**). (**E** and **F**) Molar rows in WT (**E**) and *Stim1/2*^{K14cre} mice (**F**) showing increased wear in the latter. All *Stim1/2*^{K14cre} mice analyzed in this study showed increased tooth wear. (**G** and **H**) Close up of the boxed areas in **E** and **F** showing severely cracked outer enamel in *Stim1/2*^{K14cre} mouse molars. Scale bar: 10 μm (**A–D**); 100 μm (**E** and **F**). E, enamel; D, dentine. The asterisk in **D** might be an artefact during processing of sample for SEM.

protein involved in Ca^{2+} extrusion expressed by ameloblasts, the exchanger NCKX4 (3, 17–19), was highly upregulated (Figure 4A). In WT ameloblasts, NCKX4 is localized at the apical pole of ruffled-ended ameloblasts, thus serving as a key extrusion path for Ca^{2+} (Figure 4B). By contrast, *Stim1/2*^{K14cre} ameloblasts showed a mislocalized NCKX4 expression (Figure 4B and Supplemental Figure 2), indicating abnormal trafficking of this protein, which most certainly had an effect on Ca^{2+} extrusion. These data are consistent with the essential role of SOCE in enamel mineralization, which affects the available cytosolic Ca^{2+} that can be moved by the extrusion system.

Loss of Stim1 and Stim2 causes minor changes in enamel gene expression. To analyze more broadly the effects of SOCE deficiency in ameloblasts, we isolated RNA from the EO of WT and *Stim1/2*^{K14cre} mice and analyzed global gene expression by RNA sequencing (RNAseq). We identified a total of 370 differentially expressed genes in SOCE-deficient cells, of which 114 were significantly upregulated ($P < 0.01$, absolute fold change ≥ 2), as listed in Supplemental Table 2A and illustrated in Figure 5, A and B. By comparison 256 genes were significantly downregulated ($P < 0.01$, absolute fold change ≥ 2; Supplemental Table 2B). We had previously reported that the expression of enamel genes, such as amelogenin (*Amelx*), enamelin (*Enam*), and ameloblastin (*Ambn*), is SOCE dependent based on in vitro data in which cells were stimulated with thapsigargin to passively deplete ER Ca^{2+} stores (7). Since SOCE is highly reduced in *Stim1/2*^{K14cre} mice, we had expected to detect a decrease in the expression of enamel genes.

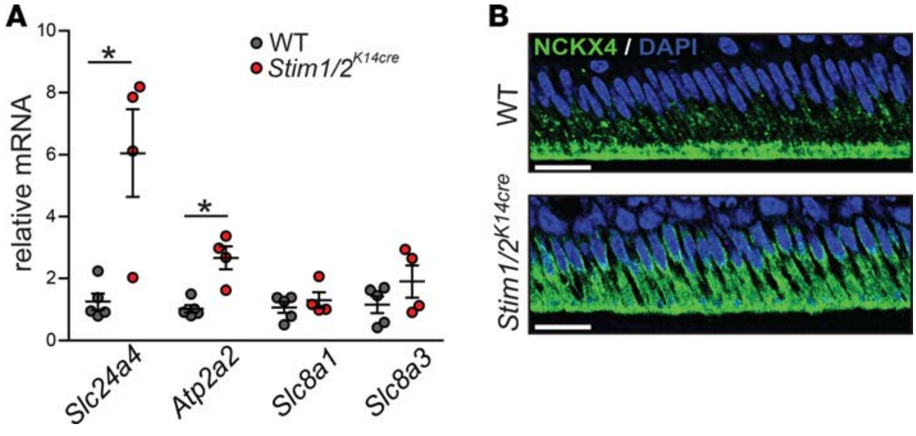

Figure 4. Changes in Ca^{2+} homeostasis in *Stim1/2*-deficient mice. (**A**) qRT-PCR analysis of the expression of Ca^{2+} handling–related genes known in enamel, including *Slc24a4*, *Atp2a2*, *Slc8a1*, and *Slc8a3*. Both *Slc24a4* (codes for NCKX4) and *Atp2a2* (codes for SERCA2) show significant upregulation, whereas *Slc8a1* and *Slc8a3* (coding for NCX1 and NCX3 respectively) did not show significant differences (mean ± SEM of $n = 5$ WT mice and $n = 4$ *Stim1/2*^{K14cre} mice; *$P < 0.01$, 1-way ANOVA with Bonferroni correction). (**B**) NCKX4 (green) cellular localization by immunofluorescence in maturation-stage ameloblasts. WT ameloblasts show apical localization of NCKX4, but, in *Stim1/2*^{K14cre} ameloblasts, its expression is visibly disrupted adopting an intracellular localization. Scale bar: 20 μm.

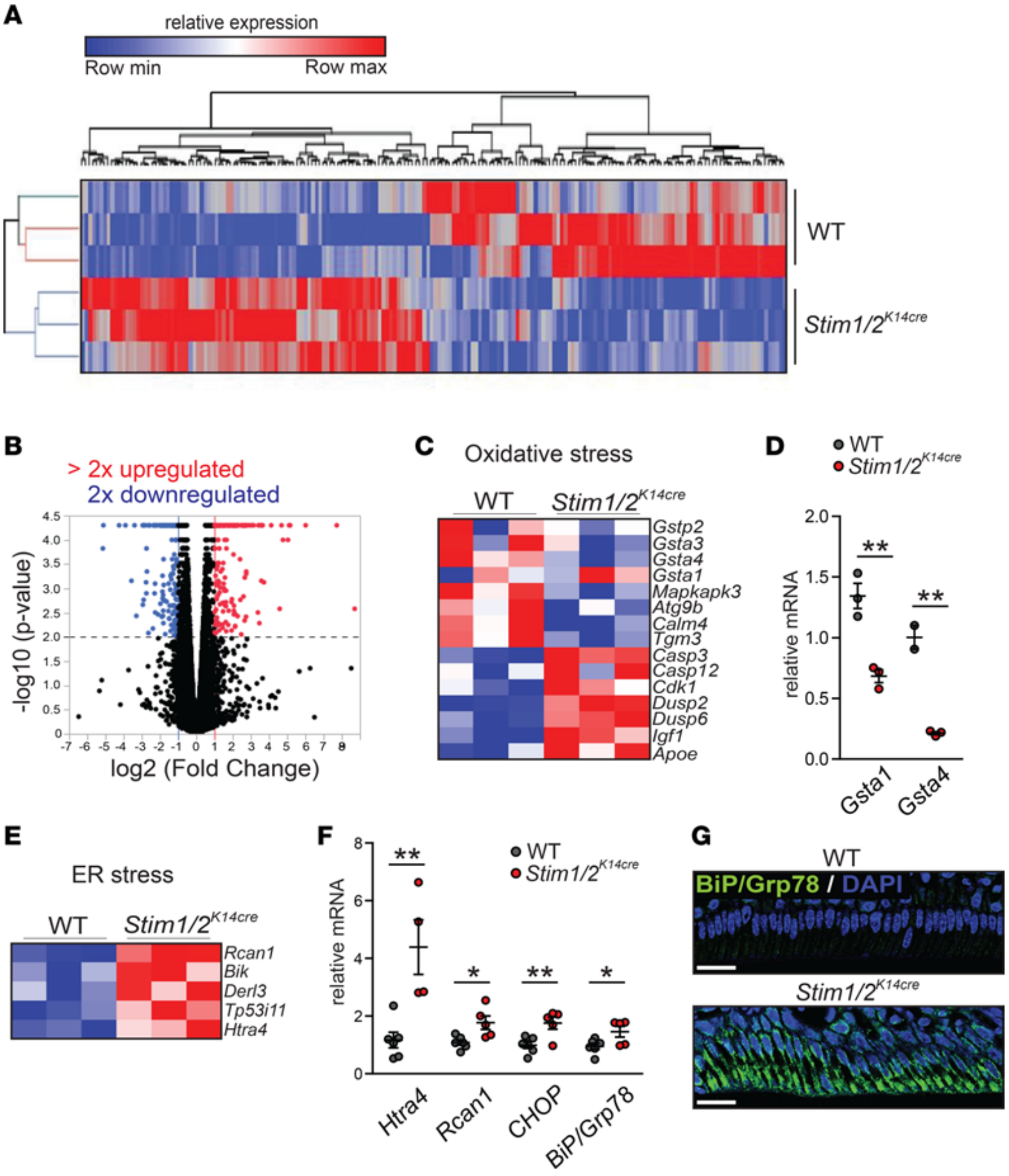

Figure 5. RNA sequencing of enamel organ cells in *Stim1/2*^{K14cre} mice highlights oxidative and endoplasmic reticulum stress. (**A**) Heatmap using 2-way hierarchical clustering of WT and *Stim1/2*^{K14cre} enamel organ cells based on the criteria described in the text. (**B**) Volcano plot of statistical significance (shown as the negative logarithm of the *P* value on the *y* axis) versus magnitude of differential gene expression (shown as the log base 2 of magnitude of mean expression difference on the *x* axis) between *Stim1/2*^{K14cre} and WT mice. The dashed line indicates a *P* value threshold of 0.01, and the vertical lines indicate absolute fold change of 2. Differentially expressed genes ($P < 0.05$, 1-way ANOVA) are shown in red (upregulation) and blue (downregulation). (**C**) Heatmap of selected genes involved in oxidative stress based on RNA sequencing (RNAseq), as described in **B**. (**D**) Analysis of oxidative stress–related enzymes glutathione S-transferases based on **C** by qRT-PCR; mean (± SEM) of $n = 3$ mice per group showing downregulation of these enzymes (**$P < 0.005$, 2-tailed unpaired Students *t* test). (**E**) Heatmap of genes involved in endoplasmic reticulum (ER) stress identified by RNAseq. (**F**) qRT-PCR analysis of ER stress–related genes showing significant upregulation of all genes; data show means (± SEM) of $n = 4$–5 mice in the *Stim1/2*^{K14cre} group and $n = 6$ mice in the WT group (*$P < 0.05$, 1-way ANOVA, **$P < 0.0125$, with Bonferroni correction). (**G**) Localization of the ER-stress associated protein BiP/Grp78 (green) by immunofluorescence in maturation-stage ameloblasts. No signals were detected in WT ameloblasts, whereas *Stim1/2*^{K14cre} maturation-stage ameloblasts showed strong signals. Scale bar: 20 µm.

The RNAseq data indicated that *Stim1/2*^{K14cre} mice showed lower but nonsignificant average values in the expression of the main enamel gene *Amelx* as well as other important genes directly associated with enamel formation (*Enam* and *Odam*) (Supplemental Figure 3, A and B). We further assessed *Amelx* expression by qRT-PCR and investigated enamel tissue sections for protein differences by immunofluorescence. Average transcript values of *Amelx* mRNA were lower but not significantly different in *Stim1/2*^{K14cre} mice (Supplemental Figure 3C). In addition, we identified weaker immunofluorescence Amelx signals in the enamel of *Stim1/2*^{K14cre} mice (Supplemental Figure 3D). These data indicate only a minor effect or no effect in enamel gene expression when disrupting SOCE.

Altered expression of genes related to oxidative stress as well as glutathione activity. To investigate the effects of SOCE deficiency in EO cells more systematically, we analyzed the RNAseq data using pathway analysis. Gene Ontology and KEGG pathway analysis showed that the oxidative stress response and glutathione metabolism pathways were the most enriched in EO cells from *Stim1/2*^{K14cre} mice (Supplemental Table 3). A summary of Ingenuity Pathway Analysis can be found in Supplemental Table 4. Specifically, cytosolic glutathione S-transferases of the α class (*Gsta1*,*Gsta4*) as well as glutathione S-transferase P, were downregulated in EO cells from *Stim1/2*^{K14cre} mice (Figure 5, C and D). Glutathione is a key indicator of changes in ROS (20). IPA also identified glutathione-mediated detoxification as being the most significantly enriched pathway ($P = 5.67^{-04}$; overlap value of 16.7%). Changes in the glutathione system had a broader effect. For example, keratins, which serve as a part of the ameloblast's cytoskeleton forming tonofilaments (tonofibrils) (21), are known to undergo S-glutathionylation (22), which can have an effect in ameloblast morphology. RNAseq data showed that mRNA

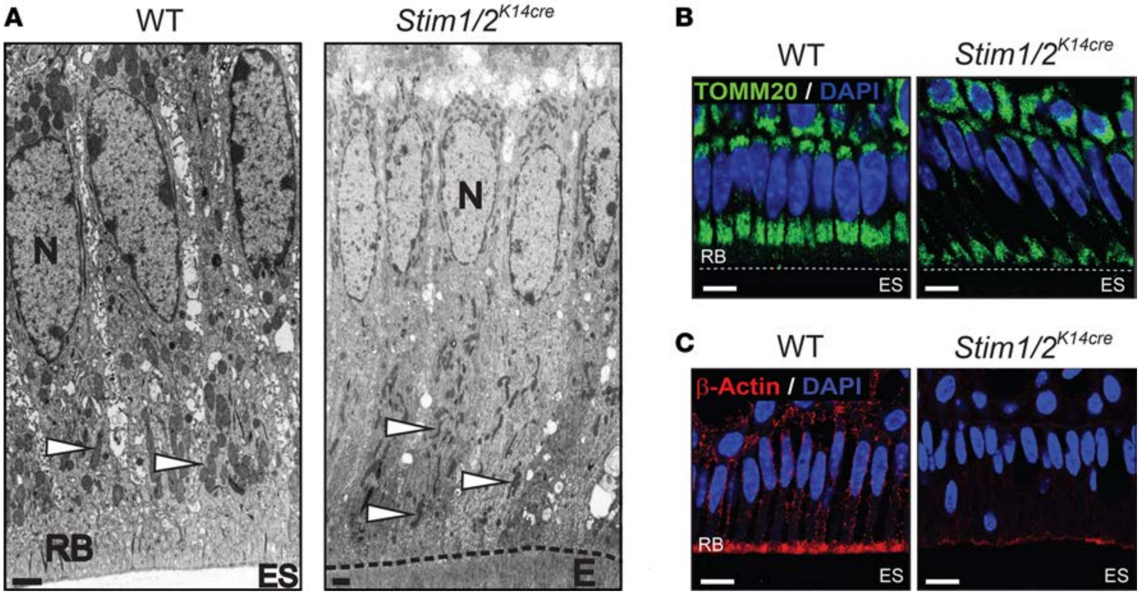

Figure 6. Altered ameloblast morphology in *Stim1/2^{K14cre}* mice. (**A**) Transmission electron microscopy images of WT and *Stim1/2^{K14cre}* maturation-stage ameloblasts showing clusters of mitochondria (arrowheads) above the ruffled border (RB) in WT ameloblasts but dispersed mitochondria in *Stim1/2^{K14cre}* ameloblasts associated with loss of RB (N, nucleus; ES, enamel space; E, enamel). Scale bar: 2 μm. (**B**) Mitochondrial localization (green) by TOMM20 immunofluorescence in maturation-stage ameloblasts of WT and *Stim1/2^{K14cre}* mice. Mitochondria are shown clustering in areas just above the RB and below the nucleus in WT cells, but this pattern is disrupted in *Stim1/2^{K14cre}* maturation-stage ameloblasts with mitochondria localized near the distal cell pole. Scale bar: 10 μm. (**C**) Cytoskeleton of *Stim1/2^{K14cre}* ameloblasts is disrupted, as evidenced by changes in immunofluorescence localization of β-actin. WT ameloblasts show actin signals strongly emanating from the apical pole and RB, but these signals are lost in *Stim1/2^{K14cre}* ameloblasts. Scale bar: 10 μm.

expression of many keratin genes was significantly downregulated in *Stim1/2*-deficient ameloblasts, including *Krt4*, *Krt13*, *Krt16*, *Krt19*, and *Krt27* (Supplemental Figure 4, A and B). In keeping with these findings, we detected abundant strands of tonofibrils in maturation-stage ameloblasts from WT mice, whereas these structures were much less abundant or did not develop in cells from *Stim1/2^{K14cre}* mice (Supplemental Figure 5). These data show that STIM1 and STIM2 control expression of genes that regulate the oxidative stress response of cells and, directly or indirectly, the expression of keratin genes.

Dysregulation of ER stress genes in Stim1/2-deficient enamel cells. Our RNAseq analysis showed that many ER stress-related genes were upregulated in ameloblasts from *Stim1/2^{K14cre}* mice compared with WT littermates. These included the serine peptidases *HtrA4* and derlin (*Derl3*) (Figure 5E). The former acts both as a protease and a chaperone in the ER reducing the amount of unfolded proteins (23) and the latter degrades misfolded glycoproteins. Regulator of calcineurin-1 (*Rcan1*), a marker for ER stress (24), was also upregulated (Figure 5E). We confirmed increased expression of *HtrA4* and *Rcan1* in *Stim1/2*-deficient cells by qRT-PCR (Figure 5F). To assess whether ER stress had caused cell death in ameloblasts from *Stim1/2^{K14cre}* mice, we performed a TUNEL assay to identify apoptotic cells but found no difference in TUNEL-positive ameloblasts derived from WT or *Stim1/2^{K14cre}* mice (Supplemental Figure 6). ER stress is associated with the unfolded protein response (UPR) system (25–27). UPR markers were activated in *Stim1/2^{K14cre}* mice. Rcan1, for example, is a direct downstream target of ATF6, one of the three main response elements during UPR activation (26). To further assess UPR activation, we performed qRT-PCR for other markers, including glucose-related protein 78 (GRP78, also known as BiP) and C/EBP homologous protein (CHOP). *BiP/Grp78* and *Chop* transcripts were significantly upregulated in EO cells from *Stim1/2^{K14cre}* mice compared with WT controls (Figure 5F), consistent with increased UPR activity. As BiP/Grp78 is the main activator of UPR, we investigated its protein expression in ameloblasts from *Stim1/2^{K14cre}* mice. Immunofluorescence analysis showed strong BiP/Grp78 expression in maturation-stage ameloblasts from *Stim1/2^{K14cre}* mice, which was absent in WT ameloblasts (Figure 5G). These data indicate increased expression of genes associated with ER stress and UPR in SOCE-deficient enamel cells.

Abnormal mitochondria in ameloblasts of Stim1/2^{K14cre} mice. Given that ER stress, particularly Rcan1 upregulation, can cause damage in mitochondria (28, 29), we investigated this possibility in *Stim1/2^{K14cre}* ameloblasts. Analysis by transmission electron microscopy of ameloblasts cells revealed important dif-

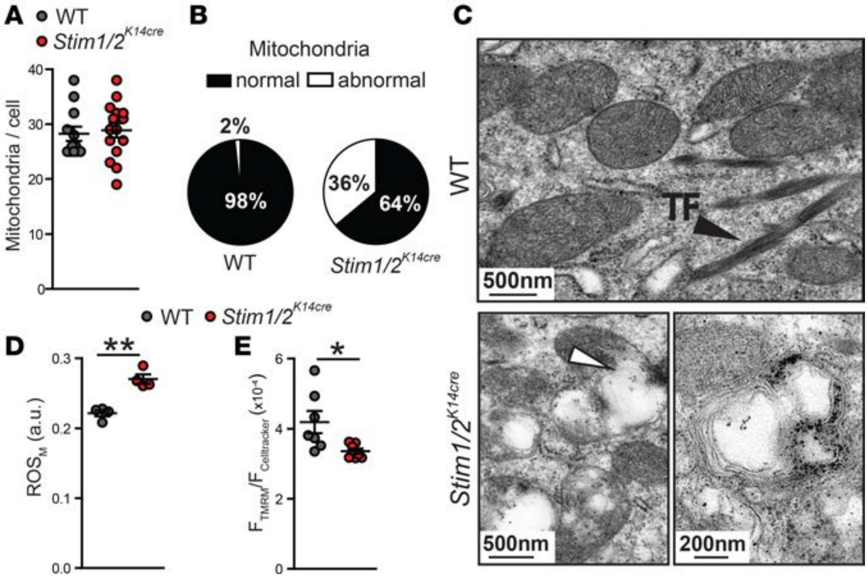

Figure 7. **Abnormal mitochondrial morphology and kinetics in store-operated Ca^{2+} entry–deficient ameloblasts.** (**A**) Ameloblast cells in WT and *Stim1/2*^{K14cre} mice show a similar number of mitochondria per section (n = 15 cells). (**B**) Increased percentage of abnormal mitochondria in *Stim1/2*^{K14cre} ameloblasts. (**C**) Transmission electron microscopy analyses of the abnormal mitochondrial phenotype in *Stim1/2*^{K14cre} ameloblasts showing a lack of well-defined cristae, presence of nonelectron dense white material (white arrowheads), and multilayered mitochondria (bottom right). The lack of tonofilaments (TF) (black arrowhead) in the mutant cells is also apparent. Scale bar: 200 nm (bottom right); 500 nm (top and bottom left). (**D**) Increased mitochondrial ROS levels detected by MitoSOX were identified in enamel cells from *Stim1/2*^{K14cre} mice. Data represent mean (± SEM) of n = 4 mice per group. Normalization was done using CellTrace (**$P < 0.005$ by 2-tailed unpaired Student's t test). (**E**) Mitochondrial membrane potential measured using TMRM showing a significant decrease in *Stim1/2*^{K14cre} enamel cells. Normalization was done using CellTrace. Data represent mean (± SEM) of n = 7 mice per group (*$P < 0.5$, 2-tailed unpaired Student's t test).

ferences in morphology as well as mitochondrial localization and appearance between WT and *Stim1/2*-deficient ameloblasts. In WT ameloblasts, the formation of infoldings of the ruffled border (RB) maintained mitochondria away from the distal cell pole so that mitochondria uniformly cluster between the RB and the nucleus around the middle of the cell (Figure 6A). *Stim1/2*^{K14cre} maturation-stage ameloblasts showed disruption of the RB enabling mitochondria to uncharacteristically spread throughout the distal pole of the cell (Figure 6A and Supplemental Figure 7). This finding was confirmed by immunofluorescence analysis using the mitochondrial import receptor TOMM20 as a marker, which showed uniform clustering of mitochondria outside the RB in WT ameloblasts but not *Stim1/2*^{K14cre} ameloblasts, in which mitochondria were located close to the distal pole of the cell (Figure 6B and Supplemental Figure 8). To further detect changes in cytoskeletal markers at the RB, we investigated the expression of actin. We found strong actin expression at the distal pole and the RB of WT ameloblasts, but a very diffuse and weak signal in *Stim1/2*-deficient ameloblasts, consistent with abnormal development of the RB in when disrupting SOCE (Figure 6C, Supplemental Figure 9).

The number of mitochondria found in *Stim1/2*^{K14cre} ameloblasts was similar to that in WT cells (Figure 7A). However, we found increased numbers of mitochondria with abnormal morphology in *Stim1/2*^{K14cre} ameloblasts (Figure 7B). These abnormal mitochondria were characterized by the presence of white (non-electron dense) material in their matrix, the absence of regular-shaped cristae, and the presence of multiple outer membranes (Figure 7C). Considering the associations between abnormal mitochondria morphology, increased production of ROS, and changes in mitochondrial bioenergetics, we investigated these possibilities. We found significantly increased mitochondrial ROS in EO cells from *Stim1/2*^{K14cre} mice compared with those from WT mice (Figure 7D). Furthermore, we observed a significant decrease in mitochondrial membrane potential (MMP) in SOCE-deficient cells (Figure 7E), suggesting abnormal mitochondrial function and a potentially reduced ability to generate ATP by oxidative phosphorylation. Taken together, these data indicate that mitochondrial function is altered in enamel cells from *Stim1/2*^{K14cre} mice. This finding is significant, as it suggests a role for mitochondrial function in enamel formation for which nearly no data are available.

Discussion

The data presented here demonstrate that *Stim1/2*^{K14cre} mice are a powerful tool for evaluating the effects of Ca^{2+} deficiency in enamel. Disrupting SOCE had a profound effect on ameloblast cells and in the composition of enamel. These data directly implicate SOCE via CRAC channels in the mineralization of dental enamel and show that ameloblasts depend on SOCE for many cellular functions. Disrupting SOCE induced the expression of genes causing ER stress and activation of the UPR. Mitochondria morphology and function were also affected.

Our results showed that the enamel of *Stim1/2*-deficient mice was thinner than that of WT controls, consistent with abnormal ameloblast function. The enamel of *Stim1/2*^{K14cre} mice produced diminished BSE-SEM signals relative to controls, which is highly consistent with decreased mineralization. This hypomineralization was also evident in the analysis of elemental composition of enamel by EDAX, showing decreased Ca content as well as alterations in other elements, including a decrease in P. Consequently, the mechanical performance of the enamel of *Stim1/2^{K14cre}* mice was extremely weak.

Ca^{2+} is the most abundant ion in the mineralized structure of enamel crystals, but how deficiencies in Ca^{2+} transport affect this tissue are poorly understood. In our study, the observed changes in the elemental composition in the enamel of *Stim1/2^{K14cre}* mice reflect the relevance of maintaining a functional Ca^{2+} transport system and the coupling of Ca^{2+} availability with other ions in the overall physiology of enamel formation.

Moreover, loss of appropriate levels of Ca^{2+} influx via SOCE affected the localization of NCKX4, the main Ca^{2+} exchanger involved in Ca^{2+} efflux in ameloblasts (17). The critical role of NCKX4 in enamel has been determined recently by studies showing that mutations in the gene encoding NCKX4 in humans and mice result in abnormal enamel that is also hypomineralized (18). In our study, by limiting Ca^{2+} influx as a consequence of disrupting SOCE, it is possible that Ca^{2+} itself, which is known to be involved in protein trafficking (30), had an effect of NCKX4. Alternatively, given that NCKX4 localizes to the ruffled-distal border of WT ameloblasts (3, 17), disruptions in the ameloblast cytoskeleton noted here dysregulated NCKX4 localization in *Stim1/2^{K14cre}* ameloblasts, likely disrupting its role in Ca^{2+} efflux. We have previously noted that NCKX4 is found in the intracellular compartment of WT smooth-ended ameloblasts (3). Thus, the intracellular localization of NCKX4 in all maturation-stage ameloblasts of *Stim1/2^{K14cre}* mice indeed suggests that these cells were unable to develop a proper RB and did not modulate from ruffled to smooth-ended cells (see also below). Therefore, the cellular infoldings of the ruffled ameloblasts are critical for NCKX4 to carry out its main function. These data are consistent with the phenotype reported in a mouse model with a mutation in WD repeat-containing protein 72 (*Wdr72*), in which NCKX4 also adopts an intracellular localization similar to what we have described here and the cyclic modulation from ruffled to smooth ameloblasts was abnormal (31).

Enamel formation is closely tied to the normal expression of a limited number of enamel matrix proteins that interact with the forming crystals to modulate growth (32). A previous study showed that the expression of these enamel genes (*Amelx*, *Ambn*, and *Enam*) was upregulated by an increase in $[Ca^{2+}]_i$ mediated by stimulation of SOCE with thapsigargin in vitro (7). By contrast, inhibiting SOCE prevented the upregulation of these genes. These studies were largely carried out in the enamel cell line LS8 but were also validated in primary EO cells (7). Here, since SOCE is disrupted in *Stim1/2^{K14cre}* mice, we had expected to detect a decrease in the expression of enamel genes. We found that both RNAseq and qRT-PCR analysis showed lower but nonsignificant differences in the average expression levels of enamel genes in mice *Stim1/2^{K14cre}* mice. We also analyzed Amelx protein expression and found weaker signals in the enamel of *Stim1/2^{K14cre}* mice. Amelx is the main protein synthesized and secreted by ameloblasts by volume (90%). These data suggest that disrupting SOCE via deletion of *Stim1* and *Stim2* genes had a minor effect on enamel genes. It is interesting, however, to note that IPA analysis identified distal-less homeobox 3 (DLX3) as one of the top upstream regulators ($P = 1.83^{-05}$). DLX3 is known as a transcription factor involved in promoting the expression of enamel genes by binding to their enhancer regions (33).

Among the top functions identified in the bioinformatics analysis and differentially expressed genes, oxidative and ER stress figured prominently. Restoring appropriate $[Ca^{2+}]_{ER}$ is critical for the ER to carry out its critical function of protein folding in preparation for transport to Golgi. Despite this noted ER stress, it is possible that the upregulation of SERCA2 in enamel cells from *Stim1/2^{K14cre}* mice may have contributed to maintaining a nonlethal level of $[Ca^{2+}]_{ER.}$ In situations of ER stress, the ER-UPR system is activated (26, 34). BiP/GRP78 is bound to the luminal domains of the 3 transmembrane signal transducers that initiate UPR (ATF6, PERK, and Ire), which remain in an inactive state in conditions of normal $[Ca^{2+}]_{ER}$ (26, 34). Accumulation of misfolded proteins releases BiP/GRP78 from this bind and instead causes it to bind to misfolded proteins (26, 34, 35). ER-UPR activation results in increased production of ER chaperones and attenuation of mRNA translation (26, 34, 35). EO cells from *Stim1/2^{K14cre}* mice showed important hallmarks of ER-UPR activation, including increased *BiP/Grp78* and *Chop*, and direct targets of the ER-UPR signal transducers, such as *Rcan1* (Figure 5, E and F). These data indicate that *Stim1/2^{K14cre}* enamel cells are sensitized to ER-UPR. ER morphology in *Stim1/2^{K14cre}* and WT ameloblasts appeared to be similar (Supplemental Figure 5), supporting our view that ER-UPR activation prevented irreparable ER damage. ER stress can affect mitochondrial function, a process that can be mediated by Rcan1. During periods of upregulation, chronic Rcan1 can lead to disruptions in mitochondrial morphology, such that it lacks clearly defined cristae and instead shows multiple inner membranes (28), as observed in many of the mitochondria in maturation-stage ameloblasts of *Stim1/2^{K14cre}* mice but not in WT counterparts (Figure 7). As the white (nonelectron dense)

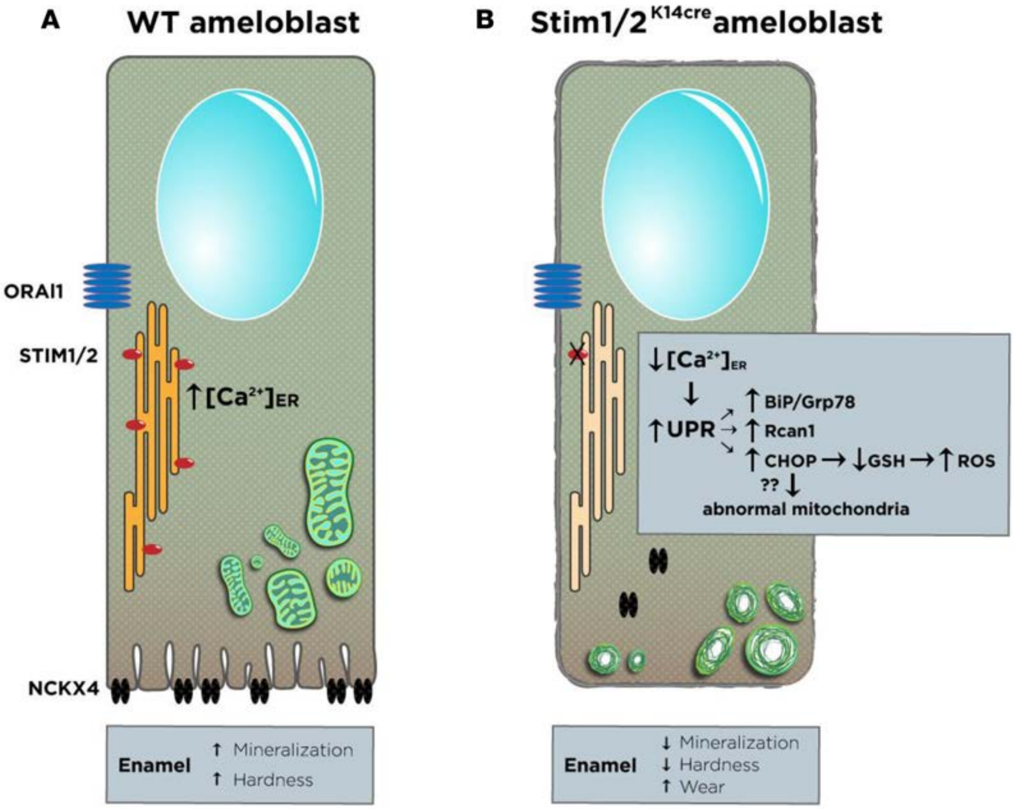

Figure 8. Schematic showing the effect of store-operated Ca^{2+} entry deficiency in enamel. (**A**) WT maturation-stage ameloblast showing a well-developed ruffled border (RB) at the apical end where the $Na^+/Ca^{2+}/K^+$ exchanger NCKX4 is localized. In these cells, depletion of endoplasmic reticulum (ER) Ca^{2+} stores results in the activation of the ER Ca^{2+} sensors STIM1 and STIM2 resulting in sustained Ca^{2+} entry via Orai1 and refilling of ER stores. Normal Ca^{2+}homeostasis and the Ca^{2+} extrusion system critically contribute to the proper mineralization of enamel. (**B**) In STIM1/STIM2–deficient cells, depletion of ER Ca^{2+}stores does not result in appropriate activation of STIM1 and STIM2, and hence Ca^{2+} entry via Orai1 is impaired, resulting in Ca^{2+}-induced ER stress. The subsequent activation of the unfolded protein response (UPR) mechanism helps mediate this cell stress and can prevent cell death. In enamel cells deficient of STIM1 and STIM2, UPR-associated genes Bip/Grp78 and RCAN1 are upregulated. CHOP is also upregulated, which can affect the glutathione system (GSH) affecting normal S-glutathionylation of actin, preventing the normal development of the RB. Mitochondria become mislocalized as a result. Mitochondria morphology is disrupted, possibly associated with RCAN1 upregulation or with a decreased glutathione system, leading to increased ROS and abnormal mitochondrial bioenergetics. Dysfunction of STIM1 and STIM2 results in severe enamel hypomineralization and softer enamel, which increases tooth wear.

areas found in the matrix of many mitochondria in *Stim1/2*^{K14cre} ameloblasts were reminiscent of mitophagy, we used the mitophagy marker LC3 but failed to show a positive immunofluorescent signal in these cells (data not shown).

The net effect of ER stress and mitochondria dysfunction commonly result in increased ROS (35) being also associated with anomalous mitochondria respiratory function resulting from abnormal mitochondria (35). Indeed EO cells from *Stim1/2*^{K14cre} mice showed significantly lower MMP and a significant increase in ROS levels compared with control cells. These data thus suggest abnormal mitochondrial function in EO cells from *Stim1/2*^{K14cre} mice and highlight the relevance of mitochondrial biology in enamel, a research area that remains poorly understood.

Mitochondrial functioning and survival is dependent on the glutathione system (36). The downregulation of a number of enzymes known as glutathione S-transferases likely decreased the cell's capacity to scavenge ROS, one of the primary functions of glutathione and S-transferases (36). Considering potential modifiers of the glutathione system in our study, it has been reported that increased levels of CHOP can have a negative effect on glutathione (25), and this might be the case in the *Stim1/2*-deficient mice. Glutathione and S-transferases are also important for the S-glutathionylation of a number of proteins with cysteine residues (35, 36). Two common target proteins of S-glutathionylation are keratins and actin (22, 37). EO cells from *Stim1/2*^{K14cre} mice showed a substantial downregulation of keratins and decreased development of tonofibrils, consistent with altered glutathione system. S-glutathionylation is also important for actin function, and dysregulation of this process can prevent the ruffling of cell membranes (37). WT ameloblasts showed strong actin signals in the RB but these signals were nearly absent in *Stim1/2*^{K14cre} ameloblasts, as they do not properly develop a distal RB. We thus suggest that changes in the glutathione system in *Stim1/2*^{K14cre} mice may have a negative effect on the cyclic modulation of ruffle to smooth-ended cells. This might provide clues concerning potential signals that trigger the cyclic modulation of ameloblasts, which, to the best of our knowledge, has only been observed in this cell type. Rather than being triggered by the external environment of the cell, as has been suggested (38), our data support a scenario in which this cyclic modulation can be activated by changes in intracellular [Ca^{2+}].

A significant outcome of this study is that in the absence of dental tissues from patients with SOCE deficiency, the *Stim1/2*^{K14cre} mice are an important tool to investigate the effects of CRAC channel deficiency in enamel, as the dental phenotype observed in *Stim1/2*^{K14cre} mice recapitulates the human phenotypes in several ways. Both showed advanced loss of enamel in teeth. This is particularly evident in our analyses, as the loss of enamel occurs in the areas of the tooth exposed to the oral environment and hence in contact with food. Patient data also suggest loss of enamel in the exposed portions of the tooth crown. Moreover, this enamel loss in the patients was linked to hypomineralization of their enamel. Here, our mouse model confirmed the hypomineralized status of enamel associated with SOCE deficiency using several biophysical approaches.

In summary, this study is the first to our knowledge to analyze the dentition of an animal model with disrupted SOCE, revealing tight associations among Ca^{2+}-induced ER stress, abnormal mitochondria, and disruption to the glutathione system, as depicted in Figure 8. We surmise that SOCE via CRAC channels is critical for the maintenance of the correct cellular machinery that provides Ca^{2+} to the forming enamel crystals. These data combined suggest that SOCE plays a number of critical roles in enamel, acting as an intracellular signaling messenger, modulator of the cell's redox state, and a provider of Ca^{2+} to be transported to the forming enamel crystals. This study significantly contributes to our understanding of CRAC channelopathy.

Methods

Mice. Mice were generated as described previously (13). Briefly, *Stim1*$^{fl/fl}$ *Stim2*$^{fl/fl}$ mice that had been previously generated as reported (14) were crossed with *K14-Cre* mice obtained from Jackson Laboratory (strain 004782). All mice were maintained on a C57BL/6 genetic background, genotyped (see Supplemental Table 5 for primers used), and used at between 6 and 16 weeks of age unless otherwise indicated. Contact SF and RSL for requests regarding *Stim1/2*^{K14cre} mice.

Primary cell culture. Primary mouse EO cells were isolated from the lower incisors as described previously (7). For single-cell suspension, EO cells were digested for 45 minutes at 37°C using Collagenase/Dispase (1 mg/ml; Roche), washed in HBSS, and transferred into X-Vivo15 medium (Lonza) containing 10%FBS, 1% Penicillin/Streptomycin (GIBCO), and 1% Glutamine (GIBCO). All experiments using EO cells were performed within 24 hours after isolation.

Immunohistochemistry. Dental tissues were obtained for immunohistochemical analysis by ventricular perfusion of 4%PFA of *Stim1/2*^{K14cre} and WT littermates. Fixed hemimandibles were decalcified with 10% EDTA for 2 weeks, embedded in paraffin, and sectioned (5-μm thick). Immunofluorescence staining was performed as described previously (39). Briefly, antigen retrieval was performed using 10 mM citric acid (pH 6.0). The following primary antibodies (all rabbit raised) were used: anti-Stim1 (1:200 dilution; Sigma-Aldrich HPA012123), anti-NCKX4 (1:500 dilution, Abcam ab136968), anti-BiP/GRP78 (1:100 dilution, Abcam ab32618), anti-TOMM20 (1:100 dilution, Abcam ab186734), anti-β-Actin (1:100 dilution, SantaCruz sc-47778), and anti-Amelx (1:50 dilution; SantaCruz; sc-32892). For amplification of primary rabbit antibodies, biotin-labeled anti-rabbit IgG (1:500 dilution, Vector Laboratories) was incubated for 1 hour. After washing, detection was carried out using Streptavidin Alexa Fluor 488 (1:800 dilution, Life Technologies). Samples were embedded using Fluoromount mounting medium (Novus) containing DAPI (Thermo Fisher Scientific). Images were taken using a Leica TCS SP5 II confocal microscope and edited using ImageJ (NIH).

$[Ca^{2+}]_i$ measurements. For $[Ca^{2+}]_i$ measurements of primary EO cells, single cells were plated overnight on a round microscope cover glass in X-Vivo Medium (containing 10% FBS). After loading cells with 1 μM Fura-2-AM (Invitrogen) for 20 minutes at room temperature, cells were washed twice in Ca^{2+}-free Ringer solution (155 mM NaCl, 4.5 mM KCl, 3 mM $MgCl_2$, 5 mM Na-HEPES, 10 mM D-glucose, pH 7.4). To exclude the possibility of fibroblast contamination, which might occur during dissection of the EO, cells were stained using a PE-conjugated anti-CD90 antibody (1:500 dilution, Biolegend). PE-positive fibroblasts were excluded from the analysis. Ca^{2+} ER store depletion was induced by perfusion of the recording chamber with 1.25 μM thapsigargin (Sigma-Aldrich) in Ca^{2+}-free Ringer solution, followed by readdition of 2 mM final extracellular Ca^{2+} concentration in Ringer solution to measure Ca^{2+} influx via SOCE. 10 μM Ionomycin (Sigma-Aldrich) was applied to test cell viability at the end of each measurement. Fluorescence measurements were recorded every 7 seconds using a Nikon 2000U Eclipse microscope. Changes in the 340/380 nm Fura-2 ratio were determined after subtracting the $[Ca^{2+}]_i$ baseline following treatment with thapsigargin.

Nanoindentation and hardness testing. Nanoindentation was performed following previously described protocols (40). Briefly, hemimandibles of 8- to 12-week-old mice were dissected, dehydrated, and embedded in methacrylate-based resin. Samples were cut into 200-mm sections using a precision diamond saw (Isomet

2000, Buehler) and attached to acrylic plates with acrylate-based cement. After 24 hours, specimens were ground and polished down to a final thickness of 150 mm. The nanoindentation test was performed using a TI 950 Triboindenter (Hysitron) equipped with a Berkovich diamond 3-sided pyramid probe. From each indentation a load-displacement curve was obtained, from which reduced modulus (measured in GPa) and hardness (measured in GPa) of enamel were computed using Hysitron TriboScan software.

Microcomputed tomography. Mandibles of 6- to 8-week-old WT and *Stim1/2*^{K14cre} mice were extracted and cleaned of soft tissues. Following dehydration in 70% ethanol at 4°C overnight, mandibles were scanned using the μCT 40 (Scanco Medical). The x-ray energy level was set at 70 kV with a slice resolution of 13 μm. All data were exported in DICOM format and imported in Amira 6.1.1 software (https://www.fei.com) for evaluation. The image data was segmented employing semiautomatic tools in order to separate the enamel from the dentine and generate 3D surface models of the teeth. The analysis of the tissue proportions was carried out for the incisor, considering a portion of tooth not affected by wear but already mineralized (Supplemental Figure 1). In particular, the part of the incisor corresponding with the first molar was identified according to the following protocol. An interpolating plane (plane 1) was set sagittally through a series of points tightly located on the superior and inferior keels of the incisor dentine, along its entire length. A plane perpendicular to plane 1 and passing through the midpoint of the mesial cervical margin of the first molar crown (plane 2) was calculated. Similarly, a third plane (plane 3) was set at the most distal point of the first molar crown. The enamel volume was obtained for the portion of incisor included between plane 2 and plane 3. The average enamel thickness was calculated by dividing the enamel volume by the area of contact between enamel and dentine.

SEM and EDAX. BSE-SEM was performed as previously described (16, 41). Briefly, mandibles of 6- to 8-week-old WT and *Stim1/2*^{K14cre} mice were extracted and cleaned of soft tissues. Following graded dehydration to 100% ethanol at 4°C, hemimandibles were embedded in polymethylmethacrylate resin (PMMA). Embedded samples were cut with a circular diamond saw at a point about 1 mm from just anterior to the mandibular first molar. Each PMMA block was polished to a 1-μm surface finish. The erupted portion was not imaged, as this was largely missing in the mutants. To detect mineralization differences, we used BSE-SEM at 50 Pa pressure using a Zeiss EVO-50 variable pressure SEM at 15 kV and 200 pA without a conductive coating. Specimens of WT and *Stim1/2*^{K14cre} mice were analyzed in parallel, setting contrast and brightness arbitrarily to accommodate high dynamic range of WT samples. Molars were also imaged for topological structure in BSE-SEM. To determine microstructural differences, samples were acid etched (phosphoric acid 37% for 5 seconds), rinsed in deionized water and coated with iridium, and analyzed in secondary electron mode. EDAX analyses were performed in a MERLIN (Zeiss) field emission SEM equipped with X-ray microanalysis using the Oxford Instruments EDS and INCA software. Comparisons were made using the WT enamel as a standard. A total of $n = 3$ mice per group were analyzed.

Transmission electron microscopy. Three WT and three *Stim1/2*^{K14cre} mouse littermates (6–8 weeks old) were perfused with 0.1 M sodium cacodylate buffer (pH 7.2) containing 1% glutaraldehyde and 4% paraformaldehyde before hemimandibles were dissected out and kept in fixative overnight. After washing for 1 hour in PBS, mandibles were immersed in decalcification solution (1.9% glutaraldehyde and 10%EDTA in 0.06 M sodium cacodylate buffer, pH 7.2) at 4°C for 2 weeks, with daily changes of the solution. Decalcified mandibles were fixed in 0.1 M sodium cacodylate buffer (pH 7.2) containing 2.5% glutaraldehyde and 2% paraformaldehyde for 2 hours at room temperature and then overnight at 4°C, using freshly made fixative. Samples were subsequently post-fixed with 1% osmium tetroxide for 1.5 hours at room temperature and then processed in a standard manner and embedded in EMbed 812 (Electron Microscopy Sciences). Semithin sections were cut at 1 μm and stained with 1% Toluidine Blue to evaluate the quality of preservation. Ultrathin sections (60 nm) were cut, mounted on copper grids, and stained with uranyl acetate and lead citrate by standard methods. Stained grids were examined under a Philips CM-12 electron microscope (FEI) and photographed with a Gatan (4 k × 2.7 k) digital camera (Gatan Inc.).

RNAseq and data processing. Two groups per genotype, with each containing cells from 3 individual mice, were analyzed for RNAseq. Whole EO was extracted and total RNA was isolated using the RNeasy Micro Kit (Qiagen). RNA quality and quantity was analyzed on a Nanodrop2000 (Fisher Scientific), and RNAseq libraries were prepared using the TruSeq RNA sample prep v2 kit (Illumina), starting with 500 ng total RNA treated with DNAse I (Qiagen), following the manufacturer's protocol. The amplified libraries (12 PCR cycles) were purified using AMPure beads (Beckman Coulter), quantified by Qubit 2.0 fluorometer (Life Technologies), and visualized in an Agilent Tapestation 2200. The libraries were pooled equimolarly, loaded on the HiSeq 4000 Sequencing System (Illumina), and run as paired-end 150-nucleotide reads generating about 50 million reads per sample. Quality control of raw sequencing reads was performed using FastQC (http://www.bioinformatics.babraham.ac.uk/projects/fastqc/). Low-quality reads, sequencing adapters, and overrepresented K-mers were removed using Trimmomatic v0.32 (42, 43). Only paired-end reads were used in subsequent analysis. Trimmed paired-end reads were aligned to the mouse genome (Ensembl release 82-GRCm38) using TopHat v2.1.0 (43) and default parameters. To calculate transcript abundances, we used Cufflinks v2.2.1 (44) to convert raw reads to FPKM values. Principal component analysis and distribution analysis were used to identify outlier samples. Differential expression analysis was performed using Cuffdiff2 (45). Data visualization was done using JMP Genomics v8 (SAS Institute) and R packages. Two-way hierarchical clustering was done using the Ward method implemented in JMP Genomics. Differences in gene expression were considered statistically significant if the adjusted P value (false discovery rate) was less than 0.01. Pathway enrichment analysis was performed using DAVID (NIH) and IPA (Qiagen) software algorithms considering genes differentially expressed between WT and *Stim1/2*^{K14cre} cells, with adjusted $P < 0.01$ and absolute fold change > 2 (listed in Supplemental Table 2, A and B). Heatmaps of selected genes were created using the conditional formatting tool in Microsoft Excel, with the highest and lowest expression for each gene displayed as red and blue (row min. and row max), respectively. Raw and processed data were deposited in GEO (accession GSE93655).

qRT-PCR. Total RNA was isolated from whole EO cells using the RNeasy Micro Kit (Qiagen) according to the manufacturer's specifications. Reverse transcription was performed using the iScript cDNA Synthesis Kit (Bio-Rad). Real-time PCR (qRT-PCR) was performed using the SsoAdvanced Universal SYBR Green qPCR Supermix (Bio-Rad) and a CFX Connect Thermocycler (Bio-Rad). *HPRT1* was used as the housekeeping gene, and relative quantification of gene expression was determined by the $2^{-\Delta\Delta CT}$ method. A complete list of all primers used in this study can be found in Supplemental Table 5.

In situ apoptosis detection. For analyzing the viability of ameloblast cells in paraffin-embedded sections we used the TACS TdT In Situ Apoptosis Detection Kit (Trevigen) following the manufacturer's instructions.

Mitochondrial superoxide measurement. ROS levels in EO cells were analyzed using MitoSOX Red (Invitrogen). Cells were plated overnight on 96-well plates. Cells were washed and kept in Ringer solution containing 5 mM pyruvate and 2 mM Ca^{2+} for 2 hours at 37°C. EO cells were incubated with 5 μM MitoSOX RED for 30 minutes at room temperature. For normalization purposes, cells were loaded in parallel with 5 μM Cell Trace violet (Invitrogen). After washing with Ringer solution, fluorescence at 450 nm and 580 nm was measured in a Flexstation 3 plate reader (Molecular Devices). The ratio of $F_{580\ nm}$ (MitoSOX) and F_{450} (Cell trace) represents relative cellular mitochondrial ROS levels. A total of $n = 4$ samples per group were analyzed.

MMP. For MMP analysis EO cells were plated overnight on a 96-well plate. Cells were then washed and kept in Ringer solution containing 5 mM pyruvate and 2 mM Ca^{2+} for 2 hours at 37°C. Tetramethylrhodamine (TMRM) (Biovision) was used in a nonquenching mode (25 nM) as described previously (46). Cells were incubated with 20 nM TMRM for 30 minutes at room temperature. For normalization purposes, cells were loaded in parallel with 5 μM Cell Trace violet (Invitrogen). After washing twice with Ringer solution, fluorescence at 450 nm and 555 nm was measured in a Flexstation 3 plate reader (Molecular Devices). The ratio of $F_{555\ nm}$ (TMRM) and F_{450} (Cell trace) represents relative MMP. A total of 7 mice per group littermates were used.

Statistics. Data were compared using 2-tailed unpaired Student's test using Prism5 (GraphPad Software) or 1-way ANOVA using SAS 9.4 software. Differences with P values of less than 0.05 were considered significant. Where appropriate, we used the Bonferroni test for multiple corrections to further analyze differences in the means. Data are represented as mean ± SEM.

Study approval. All animal procedures were conducted in accordance with protocols approved by the institutional animal care and use committees of New York University College of Dentistry and New York University Langone Medical Center.

Author contributions

ME, MV, SF, and RSL designed the study. All authors collected and analyzed data. ME, SF, and RSL wrote the paper.

Acknowledgments

This work was funded by grants DE022799 and DE025639 from the National Institute of Dental and Craniofacial Research to RSL and grant AI097302 from the National Institute of Allergy and Infectious Diseases to SF. YI is supported by New York University Abu Dhabi research grant AD105. CF was supported by A.E.R.S. Dental Medicine Organisations GmbH, Vienna, Austria (project FA547014) and the Siegfried Ludwig — Rudolf Slavicek Foundation, Vienna, Austria (project FA547016). MV was supported by a DFG fellowship (VA 882/1-1). We thank Chris Petzold and Kristen Dancel-Manning from New York University Medical Center for assistance with transmission electron microscopy, Bin Hu and Julia Katris from New York University College of Dentistry for assistance with the preparation of SEM samples, and Dindo Mijares and Pablo Atria from New York University College of Dentistry for assistance with micro-computerized tomography and hardness testing. We thank New York University Abu Dhabi Core Bioinformatics for assistance with data processing.

Address correspondence to: Rodrigo S. Lacruz, New York University College of Dentistry, 345 East 24th Street, New York, New York 10010, USA. Phone: 212.998.9433; E-mail: rodrigo.lacruz@nyu.edu.

1. Smith CE. Cellular and chemical events during enamel maturation. *Crit Rev Oral Biol Med*. 1998;9(2):128–161.
2. Smith CE, McKee MD, Nanci A. Cyclic induction and rapid movement of sequential waves of new smooth-ended ameloblast modulation bands in rat incisors as visualized by polychrome fluorescent labeling and GBHA-staining of maturing enamel. *Adv Dent Res*. 1987;1(2):162–175.
3. Nurbaeva MK, Eckstein M, Feske S, Lacruz RS. Ca2+ transport signalling in enamel cells [published online ahead of print August 11, 2016]. *J Physiol*. https://doi.org/10.1113/JP272775.
4. Hubbard MJ. Calcium transport across the dental enamel epithelium. *Crit Rev Oral Biol Med*. 2000;11(4):437–466.
5. Feske S, et al. A mutation in Orai1 causes immune deficiency by abrogating CRAC channel function. *Nature*. 2006;441(7090):179–185.
6. Prakriya M, Feske S, Gwack Y, Srikanth S, Rao A, Hogan PG. Orai1 is an essential pore subunit of the CRAC channel. *Nature*. 2006;443(7108):230–233.
7. Nurbaeva MK, Eckstein M, Snead ML, Feske S, Lacruz RS. Store-operated Ca2+ Entry Modulates the Expression of Enamel Genes. *J Dent Res*. 2015;94(10):1471–1477.
8. Nurbaeva MK, et al. Dental enamel cells express functional SOCE channels. *Sci Rep*. 2015;5:15803.
9. McCarl CA, et al. ORAI1 deficiency and lack of store-operated Ca2+ entry cause immunodeficiency, myopathy, and ectodermal dysplasia. *J Allergy Clin Immunol*. 2009;124(6):1311–1318.e7.
10. Picard C, et al. STIM1 mutation associated with a syndrome of immunodeficiency and autoimmunity. *N Engl J Med*. 2009;360(19):1971–1980.
11. Wang S, et al. STIM1 and SLC24A4 are critical for enamel maturation. *J Dent Res*. 2014;93(7 Suppl):94S–100S.
12. Lacruz RS, Feske S. Diseases caused by mutations in ORAI1 and STIM1. *Ann N Y Acad Sci*. 2015;1356:45–79.
13. Concepcion AR, et al. Store-operated Ca2+ entry regulates Ca2+-activated chloride channels and eccrine sweat gland function. *J Clin Invest*. 2016;126(11):4303–4318.
14. Oh-Hora M, et al. Dual functions for the endoplasmic reticulum calcium sensors STIM1 and STIM2 in T cell activation and tolerance. *Nat Immunol*. 2008;9(4):432–443.
15. Nurbaeva MK, et al. Dental enamel cells express functional SOCE channels. *Sci Rep*. 2015;5:15803.
16. Lacruz RS, et al. The sodium bicarbonate cotransporter (NBCe1) is essential for normal development of mouse dentition. *J Biol Chem*. 2010;285(32):24432–24438.
17. Hu P, Lacruz RS, Smith CE, Smith SM, Kurtz I, Paine ML. Expression of the sodium/calcium/potassium exchanger, NCKX4, in ameloblasts. *Cells Tissues Organs (Print)*. 2012;196(6):501–509.
18. Parry DA, et al. Identification of mutations in SLC24A4, encoding a potassium-dependent sodium/calcium exchanger, as a cause of amelogenesis imperfecta. *Am J Hum Genet*. 2013;92(2):307–312.
19. Wang S, et al. STIM1 and SLC24A4 Are Critical for Enamel Maturation. *J Dent Res*. 2014;93(7 Suppl):94S–100S.
20. Armstrong JS, et al. Role of glutathione depletion and reactive oxygen species generation in apoptotic signaling in a human B lymphoma cell line. *Cell Death Differ*. 2002;9(3):252–263.
21. Kallenbach E. Fine structure of rat incisor ameloblasts during enamel maturation. *J Ultrastruct Res*. 1968;22(1):90–119.
22. Mullen L, et al. Development of ‘Redox Arrays’ for identifying novel glutathionylated proteins in the secretome. *Sci Rep*. 2015;5:14630.
23. Clausen T, Southan C, Ehrmann M. The HtrA family of proteases: implications for protein composition and cell fate. *Mol Cell*. 2002;10(3):443–455.
24. Peiris H, et al. RCAN1 regulates mitochondrial function and increases susceptibility to oxidative stress in mammalian cells. *Oxid Med Cell Longev*. 2014;2014:520316.
25. Mekahli D, Bultynck G, Parys JB, De Smedt H, Missiaen L. Endoplasmic-reticulum calcium depletion and disease. *Cold Spring Harb Perspect Biol*. 2011;3:6.
26. Gregersen N, Bross P. Protein misfolding and cellular stress: an overview. *Methods Mol Biol*. 2010;648:3–23.
27. Malhotra JD, Kaufman RJ. The endoplasmic reticulum and the unfolded protein response. *Semin Cell Dev Biol*. 2007;18(6):716–731.
28. Ermak G, Sojitra S, Yin F, Cadenas E, Cuervo AM, Davies KJ. Chronic expression of RCAN1-1L protein induces mito-

chondrial autophagy and metabolic shift from oxidative phosphorylation to glycolysis in neuronal cells. *J Biol Chem*. 2012;287(17):14088–14098.

29. Vannuvel K, Renard P, Raes M, Arnould T. Functional and morphological impact of ER stress on mitochondria. *J Cell Physiol*. 2013;228(9):1802–1818.
30. Hay JC. Calcium: a fundamental regulator of intracellular membrane fusion? *EMBO Rep*. 2007;8(3):236–240.
31. Wang SK, et al. Critical roles for WDR72 in calcium transport and matrix protein removal during enamel maturation. *Mol Genet Genomic Med*. 2015;3(4):302–319.
32. Snead ML. Biomineralization of a self-assembled-, soft-matrix precursor: Enamel. *JOM (1989)*. 2015;67(4):788–795.
33. Zhang Z, et al. Transcriptional factor DLX3 promotes the gene expression of enamel matrix proteins during amelogenesis. *PLoS ONE*. 2015;10(3):e0121288.
34. Malhotra JD, Kaufman RJ. ER stress and its functional link to mitochondria: role in cell survival and death. *Cold Spring Harb Perspect Biol*. 2011;3(9):a004424.
35. Malhotra JD, et al. Antioxidants reduce endoplasmic reticulum stress and improve protein secretion. *Proc Natl Acad Sci USA*. 2008;105(47):18525–18530.
36. Morris G, et al. The glutathione system: a new drug target in neuroimmune disorders. *Mol Neurobiol*. 2014;50(3):1059–1084.
37. Tew KD, Manevich Y, Grek C, Xiong Y, Uys J, Townsend DM. The role of glutathione S-transferase P in signaling pathways and S-glutathionylation in cancer. *Free Radic Biol Med*. 2011;51(2):299–313.
38. Bronckers AL, Lyaruu DM, Jalali R, DenBesten PK. Buffering of protons released by mineral formation during amelogenesis in mice. *Eur J Oral Sci*. 2016;124(5):415–425.
39. Vaeth M, et al. Store-Operated Ca(2+) Entry in Follicular T Cells Controls Humoral Immune Responses and Autoimmunity. *Immunity*. 2016;44(6):1350–1364.
40. Anchieta RB, et al. Mechanical property assessment of bone healing around a titanium-zirconium alloy dental implant. *Clin Implant Dent Relat Res*. 2014;16(6):913–919.
41. Lacruz RS, et al. Requirements for ion and solute transport, and pH regulation during enamel maturation. *J Cell Physiol*. 2012;227(4):1776–1785.
42. Bolger AM, Lohse M, Usadel B. Trimmomatic: a flexible trimmer for Illumina sequence data. *Bioinformatics*. 2014;30(15):2114–2120.
43. Kim D, Pertea G, Trapnell C, Pimentel H, Kelley R, Salzberg SL. TopHat2: accurate alignment of transcriptomes in the presence of insertions, deletions and gene fusions. *Genome Biol*. 2013;14(4):R36.
44. Trapnell C, et al. Transcript assembly and quantification by RNA-Seq reveals unannotated transcripts and isoform switching during cell differentiation. *Nat Biotechnol*. 2010;28(5):511–515.
45. Trapnell C, Hendrickson DG, Sauvageau M, Goff L, Rinn JL, Pachter L. Differential analysis of gene regulation at transcript resolution with RNA-seq. *Nat Biotechnol*. 2013;31(1):46–53.
46. Abramov AY, Gegg M, Grunewald A, Wood NW, Klein C, Schapira AH. Bioenergetic consequences of PINK1 mutations in Parkinson disease. *PLoS One*. 2011;6(10):e25622.